Extraordinary strain hardening by gradient structure

XiaoLei Wu[a,1], Ping Jiang[a], Liu Chen[a], Fuping Yuan[a], and Yuntian T. Zhu[b,c,1]

[a]State Key Laboratory of Nonlinear Mechanics, Institute of Mechanics, Chinese Academy of Sciences, Beijing 100190, China; [b]Department of Materials Science and Engineering, North Carolina State University, Raleigh, NC 27695; and [c]School of Materials Science and Engineering, Nanjing University of Science and Technology, Nanjing 210094, China

Edited by Huajian Gao, Brown University, Providence, RI, and accepted by the Editorial Board April 10, 2014 (received for review December 25, 2013)

Gradient structures have evolved over millions of years through natural selection and optimization in many biological systems such as bones and plant stems, where the structures change gradually from the surface to interior. The advantage of gradient structures is their maximization of physical and mechanical performance while minimizing material cost. Here we report that the gradient structure in engineering materials such as metals renders a unique extra strain hardening, which leads to high ductility. The grain-size gradient under uniaxial tension induces a macroscopic strain gradient and converts the applied uniaxial stress to multiaxial stresses due to the evolution of incompatible deformation along the gradient depth. Thereby the accumulation and interaction of dislocations are promoted, resulting in an extra strain hardening and an obvious strain hardening rate up-turn. Such extraordinary strain hardening, which is inherent to gradient structures and does not exist in homogeneous materials, provides a hitherto unknown strategy to develop strong and ductile materials by architecting heterogeneous nanostructures.

gradient structured metal | nanocrystalline metal

Mankind has much to learn from nature on how to make engineering materials with novel and superior physical and mechanical properties (1, 2). For examples, the clay-polymer multilayers mimicking naturally grown seashells are found to have exceptional mechanical properties (3). Another example is the gradient structure, which exists in many biological systems such as teeth and bamboos. A typical gradient structure exhibits a systematic change in microstructure along the depth on a macroscopic scale. Gradient structures have been evolved and optimized over millions of years to make the biological systems strong and tough to survive nature. They are greatly superior to manmade engineering materials with homogeneous microstructures.

Here we report the discovery of a hitherto unknown, to our knowledge, strain hardening mechanism, which is intrinsic to the gradient structure in an engineering material. The gradient structure shows a surprising extra strain hardening along with an up-turn and subsequent good retention of strain hardening rate. Strain hardening is critical for increasing the material ductility (4–6). We also show a superior ductility–strength combination in the gradient structure that is not accessible to conventional homogeneous microstructures.

Microstructural Characterization of Gradient Structure

We demonstrate these behaviors in a grain-size gradient-structured (GS) sample, i.e., two GS surface layers sandwiching a coarse-grained (CG) core, produced by the surface mechanical attrition treatment (SMAT) (7) in a 1-mm-thick CG interstitial free (IF)-steel sheet (*SI Materials and Methods*). The GS layers on both sides have a gradual grain-size increase along the depth (Fig. 1*A*). In the outermost layer of ∼25-μm thickness are nearly equiaxial nanograins with a mean size of 96 nm (Fig. 1*B*). The grain size increases gradually to 0.5 and 1 μm at the depths of ∼60 and 90 μm, respectively, with subgrains or dislocation cells smaller than 100 nm. For convenience, we define the top 90-μm-depth as a nanostructured layer (8–10) with a grain-size gradient. The whole gradient layer is 120 μm thick, including the deformed CG layer with either dislocation tangles or dislocation cells of sizes ranging from submicrometers to micrometers. The central strain-free CG core has an average grain size of 35 μm (Fig. 1*C*).

Unique Mechanical Responses Under Uniaxial Tension

Fig. 2*A* shows the engineering stress–strain (σ_e–ε_e) curves. The gradient-structured (GS–CG) sample exhibits not only a large tensile uniform elongation (E_U), comparable to that of the homogeneous CG sample, but also yield strength that is ∼2.6 times as high. In contrast, the freestanding nanostructured (NS) film becomes unstable soon after yielding. Interestingly, the GS–CG sample shows a transient hardening in the regime of small tensile strains on its σ_e–ε_e curve between two inflection points (Fig. 2*B*, *Inset*). This caused an up-turn in the strain hardening rate Θ (Fig. 2*B*, *Inset*). Meanwhile, the unloading–reloading σ_e–ε_e curves also reveal a similar Θ-up-turn upon each reloading (GS–CG$^+$, red curves in Fig. 2*B*). More importantly, the GS–CG sample shows an even slower Θ-reduction than that of the CG sample (Fig. 2*B*), indicating a better Θ-retention in the GS–CG sample. In contrast, the freestanding GS layer and CG core do not show any Θ-up-turn (see the GS layer and CG curves in Fig. 2*B*), suggesting that the unique behavior is produced only when these two types of layers form an integral bulk.

The dramatic hardening behavior raises a critical issue: where in the GS–CG sample is strain hardening generated? To answer this question, we measured the microhardness (H) along the depth of GS–CG samples after testing them to varying strains. As shown in Fig. 2*C*, the H values increase with increasing tensile strain. The border, where H values in the untested sample no longer drop, demarcates the GS layer and CG core. Fig. 2*D* shows H increments, ΔH, along the depth caused by testing at various tensile strains. ΔH is an indicator on the magnitude of

Significance

Nature creates the gradient structure (GS) for a purpose: to make biological systems strong and tough to survive severe natural forces. For the grain-size GS, the deformation physics is still unclear. One wonders if the grain-size GS in the nano-microscale would also benefit materials engineered by mankind. In this paper, a universal strain hardening mechanism is revealed in the GS. We discovered a unique extra strain hardening that is intrinsic to the GS. Its mechanism is the presence of strain gradient together with the stress state change. A superior combination of strength and ductility that is not accessible to conventional homogeneous materials is obtained. As a novel mechanism, extra strain hardening renders high ductility in the GS materials.

Author contributions: X.W. designed research; X.W., P.J., and L.C. performed research; X.W., P.J., L.C., F.Y., and Y.T.Z. analyzed data; and X.W. and Y.T.Z. wrote the paper.

The authors declare no conflict of interest.

This article is a PNAS Direct Submission. H.G. is a guest editor invited by the Editorial Board.

Freely available online through the PNAS open access option.

[1]To whom correspondence may be addressed. E-mail: xlwu@imech.ac.cn or ytzhu@ncsu.edu.

This article contains supporting information online at www.pnas.org/lookup/suppl/doi:10.1073/pnas.1324069111/-/DCSupplemental.

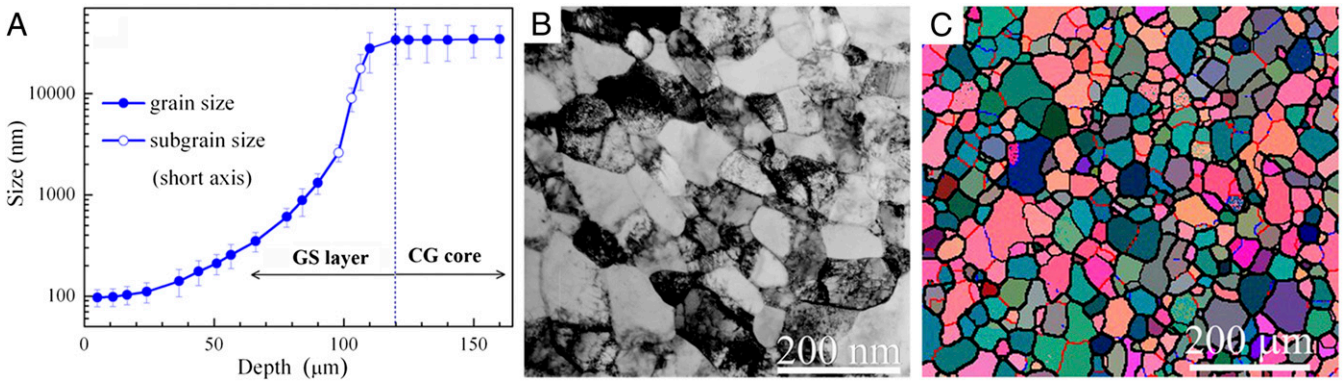

Fig. 1. Gradient structure by SMAT. (*A*) Variation of average grain sizes along the depth. The error bars represent the SD of the grain sizes. The GS sample was produced by means of SMAT for 5 min on both sides of a CG IF-steel sheet. (*B*) Cross-sectional TEM bright-field image of the nanograins with a mean grain size of 96 nm at the depth of ~10 μm. (*C*) Electron back-scatter diffraction image of coarse grains with a mean grain size of 35 μm.

hardening retained after unloading. For comparison, the ΔH values are also measured in both the freestanding GS layer (failure strain of 0.05 in Fig. 2*A*) and homogeneous CG after tensile testing them to the strain of 0.05. Remarkably, the layer in GS–CG exhibits a unique extra strain hardening, i.e., a much higher ΔH than that of the freestanding GS layer (dotted area in Fig. 2*D*). This extra hardening originates in the gradient layer, and its peak moves inward and finally penetrates into the CG core at higher strains. This indicates again that the gradient layer needs to form an integral bulk with the CG core to be effective in producing strain hardening.

The above unique hardening behavior is inherent to the GS–CG and is caused by the gradient-generated multiaxial stresses and strain gradient. Under uniaxial tension (Fig. 3*A*), necking instability readily occurs in the NS surface layers at very low tensile strains (see the NS-film curve in Fig. 2*A*), which is characterized by their fast lateral shrinking. However, lateral instability is constrained and quickly stopped by the neighboring stable layer. Consequently, the strain gradient is produced near the border between the unstable surface layers and the stable central core (11, 12), where strain continuity is required to keep material continuity.

The mutual constraint between the unstable surface layers and stable central core leads to stress state changes, as schematically shown in Fig. 3*A*. When the shrinking surface layers are constrained by the central core, the constraint is realized in the form of lateral tensile stress in the surface layers, i.e., (σ_x^+) as shown

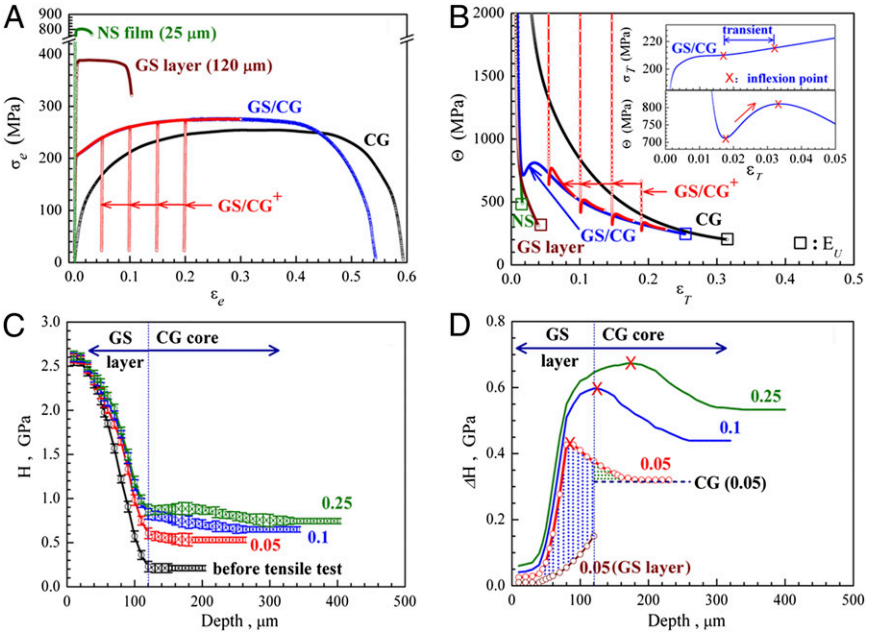

Fig. 2. Hardening rate up-turn and unique extra strain hardening. (*A*) Tensile engineering stress–strain (σ_e–ε_e) curves at a quasistatic strain rate of 5×10^{-4} s^{-1}. CG: standalone homogeneous CG sample; GS layer: grain-size GS layer of 120-μm thickness; GS–CG: sandwich sample of 1-mm thickness. NS: freestanding, quasihomogeneous nanostructured film of 20-μm thickness peeled from the top surface of GS; GS–CG$^+$: the same sandwich sample subjected to unloading–reloading tensile testing at four separate strains of 0.05, 0.1, 0.15, and 0.2. All tensile samples were dog-bone-shaped, with a gauge dimension of 8 mm × 2.5 mm. (*B*) Strain hardening rate ($\Theta = d\sigma/d\varepsilon$) vs. true strain ($\varepsilon_T$) curves. (*Inset*) Transient response on the σ_T–ε_T curve of the GS–CG sample between two inflection points marked by "×," corresponding to the Θ-up-turn on its Θ–ε_T curve. GS–CG$^+$ (red curve) shows Θ-up-turn upon each reloading. (*C*) Vickers microhardness (H) vs. depth. The H values were measured on the cross-sectional GS–CG sample after tensile testing them to varying strains (labeled on the curves). The border between GS layer and CG core is located at 120-μm depth. (*D*) ΔH (H increment) vs. depth after varying tensile strains. The dotted area indicates the extra hardening in the GS–CG sample.

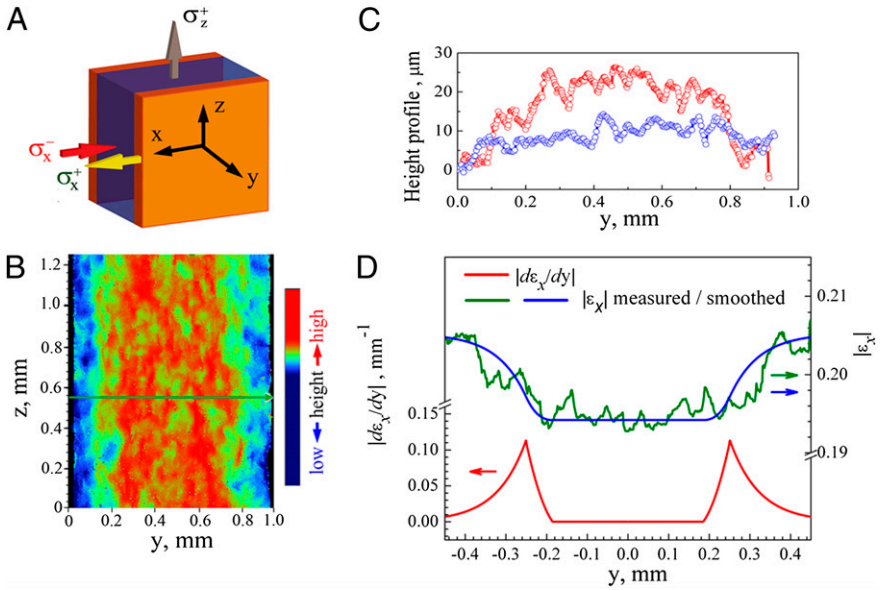

Fig. 3. Stress state change and strain gradient. (*A*) Schematic stress state change during uniaxial tension in a GS–CG sample. Outer layers: the plastically unstable layers. Core: the stable layer. σ_x^+ is the lateral tensile stress in the outer layers, and σ_x^- is the lateral compressive stress in the inner layer in the *x* direction. σ_z^+ is the applied uniaxial stress. (*B*) Measured height contour on the side surface, vertical to the *x* axis, within the gauge section of GS–CG sample at the tensile strain of 0.25. (*C*) Measured height profiles covering the thickness of both GS–CG sample (along the green line in *B*) and a standalone homogeneous CG sample after tensile testing to a strain of 0.3. (*D*) Distribution of lateral strain (ε_x) and strain gradient ($d\varepsilon_x/dy$) across the thickness along the green line in *B*.

Fig. 3*A*. Because no external lateral stress is applied to the sample, the tensile stresses in the outer surface layers have to be balanced by a lateral compressive stress (σ_x^-) in the inner stable core. Therefore, the applied uniaxial tensile stress is converted to complex 2D stress states with the outer surface layers under a tension–tension stress state and the central stable layer under a tension–compression stress state.

To evaluate the strain gradient, the height profiles on the lateral surface, i.e., vertical to the *x* axis in Fig. 3*A*, were measured after suspension of a tensile testing at the strain of 0.25, as shown in Fig. 3*B* (also Fig. S1*A*). The GS–CG sample exhibits marked height difference, i.e., lower on both sides and higher in the middle (see the red curve in Fig. 3*C*) (also Fig. S1*B*). This is the direct evidence that nonuniform lateral deformation in GS–CG occurred, with the outer GS layers shrunk more than the central zone. In contrast, a homogeneous standalone CG sample only shows surface roughness without a systematic height difference (see the blue curve in Fig. 3*C*). The lateral strain ε_x was calculated as $\varepsilon_x = \delta x/x_0$, where $\delta x = x - x_0$ was measured from the contour (Fig. 3*C*) and x_0 is the initial width. This strain is negative due to shrinking, and the distribution of its absolute values along the green line in Fig. 3*B* is plotted in Fig. 3*D*. It is also fitted with a smooth curve $\varepsilon_x(y)$ (blue curve). As shown, the absolute value of ε_x is essentially unchanged in the stable central layer except for the effect of surface roughness. However, the $|\varepsilon_x|$ increases gradually toward the surface, which produces strain gradient $d\varepsilon_x/dy$ across the sample thickness as plotted in Fig. 3*D* (red curve). As shown, there exists a maximum strain gradient near the interface. As discussed later, this maximum strain gradient will promote the accumulation of geometrically necessary dislocations (GNDs) (11,12) to produce a peak of extra strain hardening.

To probe the physical origin behind the Θ-up-turn, dislocation evolution with strains in GS sample is studied by stress relaxation tests, which is complemented by transmission electron microscopy (TEM) observations. Fig. 4*A* shows a σ_e–ε_e curve as a function of relaxation time at varying strains (Fig. 4*A*, *Inset*), which were selected carefully to cover the strain range where the Θ-up-turn occurs (Fig. 2*B*, *Inset*). The ratio $\mathrm{Re} = \rho_m/\rho_{m0}$ represents the relative mobile dislocation density evolution (13). Fig. 4*B* shows the evolution of the ρ_m/ρ_{m0} with relaxation time and its inset reveals how the ρ_m/ρ_{m0} varies with tensile strain. As shown, with increasing tensile strain, the Re first drops (Fig. 4*B*, *Inset*) and then reaches the minimum value at the strain of 0.015, after which Re increases rapidly to reach a near-saturated value at the strain of 0.05. Interestingly, the strain value of 0.015 almost coincides with the strain at which minimum Θ is observed in the GS–CG sample (Fig. 2*B*, *Inset*). This observation indicates rapid exhaustion of mobile dislocations at low strains, which is consistent with what was reported in nanocrystalline Ni (14). In addition, the strain of 0.015 is also near the onset of necking instability for the NS film (see the green curve in Fig. 2*A*), suggesting that the exhaustion of mobile dislocations promoted instability of the GS layers (15). On the other hand, this also creates more space for dislocation accumulation later, setting the stage for Θ-up-turn (Fig. 4*E*).

TEM observations provide us with information on the evolution of dislocation structures in the nanograins. At very small strain of 0.008 (soon after yielding), tangled high-density dislocations are visible either in their interior or at boundaries and subboundaries (Fig. 4*C*). At higher strain of 0.015 (before the Θ-up-turn), debris of dislocations is visible (Fig. 4*D*), indicating the occurrence of disentanglement and annihilation of the initial dislocation structure (16). Further increasing strain to 0.035 (soon after Θ-up-turn) regenerates dislocation structures (Fig. 4*E*). These observations are consistent with and provide insight into the evolution of mobile dislocations and Θ-up-turn in the GS–CG sample.

Discussion and Summary

The extra strain hardening (Fig. 2*D*) is caused by the strain gradient (Fig. 3*D*), which needs to be accommodated by the generation of the GNDs (17–20). The GNDs interact and tangle with mobile dislocations to further promote the dislocation storage (18). These dislocation activities effectively promote the dislocation accumulation near the border demarcating the unstable and stable layers, which produces the observed extra hardening (ΔH) peak as shown in Fig. 2*D*. With increasing applied

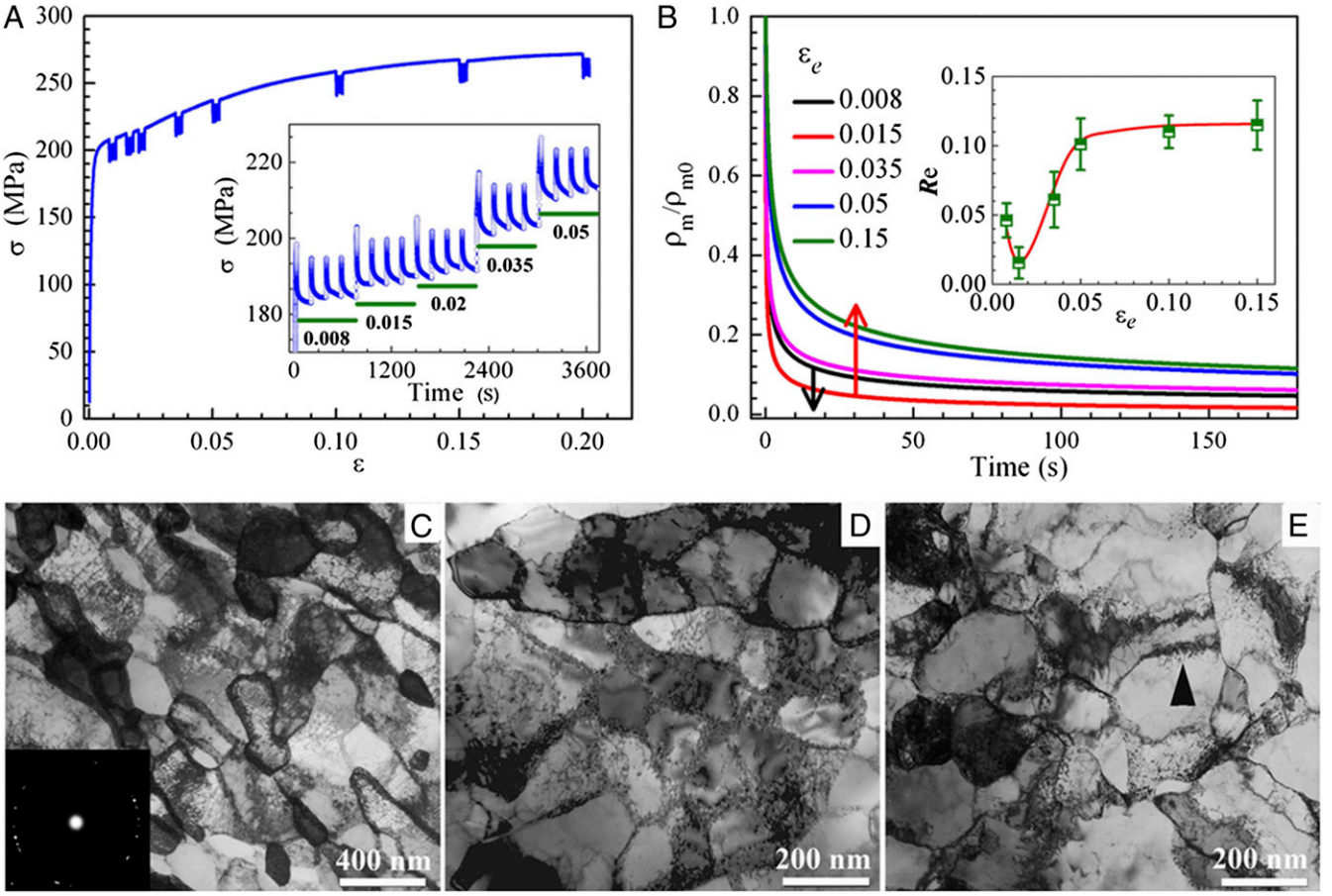

Fig. 4. Evolution in mobile dislocation density. (*A*) σ_e–ε_e curve from a stress relaxation test at eight starting strains. (*Inset*) Stress–relaxation time curve. Four relaxation tests are performed at each starting strain. (*B*) Evolution of the mobile dislocation density ρ_m/ρ_{m0} with the first stress relaxation (180 s) at varying starting strains. ρ_m is the mobile dislocation density, whereas ρ_{m0} is the dislocation density at the onset of each relaxation cycle. Two arrows indicate the first drop and later rise in ρ_m/ρ_{m0} with strain. (*Inset*) $R_e = \rho_m/\rho_{m0}$ after relaxation as a function of starting strain. *(C–E)* Cross-sectional TEM bright-field images of GS–CG samples after suspension of tensile testing at varying strains. (*C*) Dislocation-tangled grain boundaries and subboundaries at the strain of 0.008 (~20 μm deep). (*D*) Dislocation debris left inside grain interior and on their boundaries at the strain of 0.015 (~20 μm deep). (*E*) Newly formed dislocation subboundaries (indicated by a triangle) at the strain of 0.035 (~25 μm deep).

strain, stable layers will become unstable, which leads to migration of the border and consequently the ΔH peak toward the CG core. This leaves in its wake high densities of dislocations. This explains why the ΔH peak becomes flatter and moves inward as the tensile strain increases. In other words, the extra strain hardening is accumulative with the dynamically moving border. This is the reason why the GS–CG sample has a slower decrease in Θ than the homogeneous CG core with strain (Fig. 2*B*). Furthermore, the multiaxial stress state will activate more slip systems (16, 21), which makes it more likely for dislocations to interact and entangle with each other (Fig. 4*E*), following the initial depletion of dislocations (Fig. 4*B*). The GNDs caused by the strain gradient and the dislocation accumulation caused by the multiaxial stress state are the primary causes for the observed dramatic hardening rate up-turn and its good retention.

The nanograined layers play critical roles in producing high extra strain hardening although no significant extra hardening occurs in the nanograined layers themselves (Fig. 2*D*). First, the nanograined layers have a much higher flow stress than the larger-grained inner layer. This ensures high lateral stresses (Fig. 3*A*) during necking instability of the nanograined layer, which is constrained by the stable central layer. The high lateral stress will promote the operation of additional slip systems to help with dislocation storage. Second, the early necking by the nanograined layers activates the multiaxial stresses and strain gradient at an early stage of the mechanical testing, which consequently starts the extra strain hardening process in an early stage.

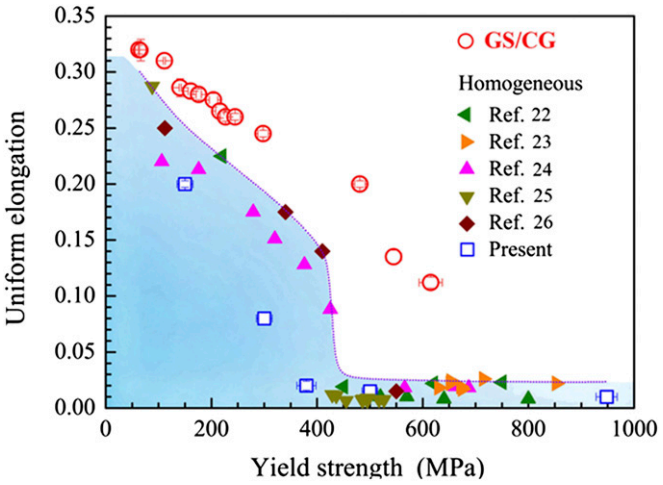

Fig. 5. Superior mechanical property. Strength and ductility in the GS–CG samples of IF-steel compared with their homogeneous counterparts.

Our preliminary results also suggest that there is a minimum SMAT processing time above which the strain hardening rate upturn occurs. This minimum time is associated with a minimum GS layer thickness. It is our hypothesis that there should be an optimum GS layer thickness that produces the most significant Θ-up-turn and the most extra strain hardening. Further systematic investigation is needed to verify this hypothesis. Also note that the mechanism for good ductility observed here is totally different from that in gradient nanograined Cu (8), where high ductility was attributed to grain growth due to the low structural stability of the nanograined Cu. No grain growth is observed in the GS IF-steel in the current study (Fig. S2).

Due to the extra strain hardening, the gradient structure provides for an effective route to a superior combination of good ductility and high strength (Fig. 5). When the homogeneous IF-steel is deformed to increase strength, its ductility usually drops dramatically, especially when the strength is above 400 MPa (22–26). In contrast, the ductility of GS sample is 5–10 times higher than that of the homogeneous nanograined structures within the strength range of 450–600 MPa. More importantly, the GS sample can be easily produced in metallic materials in a cost-effective and large-scale way and therefore is expected to be conducive to industrial production.

ACKNOWLEDGMENTS. X.W., P.J., L.C., and F.Y. are funded by the National Natural Science Foundation of China (11072243, 11222224, 50571110, and 11021262) and 973 Program of China (2012CB92203, 2012CB937500 6138504). Y.T.Z. is funded by the US Army Research Office under Grants W911NF-09-1-0427 and W911QX-08-C-0083 and by the Nanjing University of Science and Technology.

1. Suresh S (2001) Graded materials for resistance to contact deformation and damage. *Science* 292(5526):2447–2451.
2. Gao HJ, Ji BH, Jager IL, Arzt E, Fratzl P (2003) Materials become insensitive to flaws at nanoscale: Lessons from nature. *Proc Natl Acad Sci USA* 100(10):5597–5600.
3. Miserez A, Schneberk T, Sun CJ, Zok FW, Waite JH (2008) The transition from stiff to compliant materials in squid beaks. *Science* 319(5871):1816–1819.
4. Wang YM, Chen MW, Zhou FH, Ma E (2002) High tensile ductility in a nanostructured metal. *Nature* 419(6910):912–915.
5. Lu K, Lu L, Suresh S (2009) Strengthening materials by engineering coherent internal boundaries at the nanoscale. *Science* 324(5925):349–352.
6. Ritchie RO (2011) The conflicts between strength and toughness. *Nat Mater* 10(11): 817–822.
7. Lu K, Lu J (1999) Surface nanocrystallization (SNC) of metallic materials-presentation of the concept behind a new approach. *J Mater Sci Technol* 15(3):193–197.
8. Fang TH, Li WL, Tao NR, Lu K (2011) Revealing extraordinary intrinsic tensile plasticity in gradient nano-grained copper. *Science* 331(6024):1587–1590.
9. Zhu YT, Langdon TG (2004) The fundamentals of nanostructured materials processed by severe plastic deformation. *JOM* 56(10):58–63.
10. Huang XX, Hansen N, Tsuji N (2006) Hardening by annealing and softening by deformation in nanostructured metals. *Science* 312(5771):249–251.
11. Ashby MF (1970) The deformation of plastically non-homogeneous materials. *Philos Mag* 21(170):399–424.
12. Gao H, Huang Y, Nix WD, Hutchinson JW (1999) Mechanism-based strain gradient plasticity - I. Theory. *J Mech Phys Solids* 47(6):1239–1263.
13. Caillard D, Martin JL (2003) *Thermally Activated Mechanisms in Crystal Plasticity* (Pergamon, Amsterdam), pp 15–25.
14. Wang YM, Hamza AV, Ma E (2005) Activation volume and density of mobile dislocations in plastically deforming nanocrystalline Ni. *Appl Phys Lett* 86:241917.
15. Wang YM, Ma E (2004) Three strategies to achieve uniform tensile deformation in a nanostructured metal. *Acta Mater* 52(6):1699–1709.
16. Wilson DV (1994) Influences of cell-walls and grain-boundaries on transient responses of an IF steel to changes in strain path. *Acta Metall Mater* 42(4):1099–1111.
17. Nix WD, Gao HJ (1998) Indentation size effects in crystalline materials: A law for strain gradient plasticity. *J Mech Phys Solids* 46(3):411–425.
18. Gao HJ, Huang YG (2003) Geometrically necessary dislocation and size-dependent plasticity. *Scr Mater* 48(2):113–118.
19. Hughes DA, Hansen N, Bammann DJ (2003) Geometrically necessary boundaries, incidental dislocation boundaries and geometrically necessary dislocations. *Scr Mater* 48(2):147–153.
20. Hansen N, Huang X (1998) Microstructure and flow stress of polycrystals and single crystals. *Acta Mater* 46(5):1827–1836.
21. Asaro RJ (1983) Micromechanics of crystals and polycrystals. *Adv Appl Mech* 23:1–115.
22. Tsuji N, Ito Y, Saito Y, Minamino Y (2002) Strength and ductility of ultrafine grained aluminum and iron produced by ARB and annealing. *Scr Mater* 47(12):893–899.
23. Huang XX, Kamikawa N, Hansen N (2008) Increasing the ductility of nanostructured Al and Fe by deformation. *Mater Sci Eng A* 493(1-2):184–189.
24. Purcek G, Saray O, Karaman I, Maier HJ (2012) High strength and high ductility of ultrafine-grained interstitial-free steel produced by ECAE and annealing. *Metall Mater Trans, A Phys Metall Mater Sci* 43A(6):1884–1894.
25. Lapovok R, et al. (2012) Asymmetric rolling of interstitial-free steel using one idle roll. *Metall Mater Trans, A Phys Metall Mater Sci* 43A(4):1328–1340.
26. Hazra SS, Pereloma EV, Gazder AA (2011) Microstructure and mechanical properties after annealing of equal-channel angular pressed interstitial-free steel. *Acta Mater* 59(10):4015–4029.

Supporting Information

Wu et al. 10.1073/pnas.1324069111

SI Materials and Methods

1. Material and Heat Treatment. A 1-mm-thick interstitial free (IF)-steel sheet was used in the present study. Its composition is (wt %) 0.003% C, 0.08% Mn, 0.009% Si, 0.008% S, 0.011% P, 0.037% Al, 0.063% Ti, and 38 ppm N. Sample disks with a diameter of 100 mm were cut from the IF-steel sheet and then preannealed at 1,173 K for 1 h to obtain a homogeneous coarse-grained microstructure with a mean grain size of 35 μm.

2. Producing Grain-Size Gradient Structures via Surface Mechanical Attrition Treatment. The technique of the surface mechanical attrition treatment (SMAT) (1) was used to process the gradient-structured–coarse-grained (GS–CG) sandwich samples with grain-size GS layers on both surfaces of the CG core in IF-steel. The SMAT technique is based on the impaction of spherical shots (4–6 mm) on the sample disk using high-power ultrasound. Because of the high frequency of the system (20 kHz), the entire surface of the component is peened with a very high number of impacts over a short period of time. The SMAT processing time was the same for both sides of each disk, which varied from 40 s to 15 min. No crack was observed on the sample surface after SMAT processing.

3. Tensile Test, Unloading-Reloading Test, and Stress–Relaxation Test. Tensile specimens with a gauge length of 8 mm and a width of 2.5 mm were cut from SMAT-processed sample disks. The nano-grained films for Fig. 1*A* were prepared by polishing away the 5-min SMAT-processed samples from one side only, leaving behind a film of desired thickness for tensile testing.

i) Quasistatic uniaxial tensile tests were carried out using an Instron 5582 testing machine at a strain rate of $5 \times 10^{-4}\cdot s^{-1}$ at room temperature. An extensometer was used to measure strain during the period of uniform tensile deformation.

ii) Loading–unloading tests were conducted using an Instron 5966 testing machine at room temperature. Four loading–unloading cycles were conducted during a uniaxal tensile test, at tensile strains of 5%, 10%, 15%, and 20%, respectively. Upon straining to certain value (e.g., 5%) at strain rate of $5 \times 10^{-4}\cdot s^{-1}$, the specimen was unloaded by the stress-control mode to 20 N at unloading rate of 200 $N\cdot min^{-1}$, followed by reloading at a strain rate of $5 \times 10^{-4}\cdot s^{-1}$ to the same applied stress before the next unloading.

iii) Stress–relaxation uniaxial tensile tests were performed using an Instron 5966 testing machine under strain-control mode at room temperature at eight initial applied strains, i.e., 0.8% 1.5%, 2%, 3.5%, 5%, 10%, 15%, and 20%. Upon reaching any strain at a strain rate of $5 \times 10^{-4}\cdot s^{-1}$, the strain was maintained constant whereas the stress was recorded as a function of time. After the first relaxation over an interval of 180 s, the specimen was reloaded by a strain increment of 0.6% at a strain rate of $1 \times 10^{-4}\cdot s^{-1}$ for the next relaxation. Four stress relaxations were conducted at 0.8%, and then the specimen was strained to next strain at a strain rate of $5 \times 10^{-4}\cdot s^{-1}$. The relaxation and reloading cycles were then performed with the same testing parameters used at 0.8%, including the number of cycles, the duration of each relaxation, and the strain increment and strain rate during reloading. To obtain reproducible experimental results, the stress relaxations were carried out at least four times. The method to calculate the mobile dislocation density can be found in SI section 6.

4. Height Profile Measurements. The quantitative and 3D surface height profiles in a large area were measured by means of a noncontact Bruker Contour-I white light interferometry operated in a vertical scanning interferometry mode. The maximum resolution in depth was 0.02 μm. The measured data are shown in Fig. S1.

5. Transmission Electron Microscopy Observations. Cross-sectional transmission electron microscopy (TEM) observations were conducted to investigate the microstructural evolution and grain-size distribution in the GS. TEM samples were cut from a gauge section of the tensile sample, and at a depth of ~5 μm from the surface. Dozens of TEM micrographs was taken from each sample, and over 500 grains were measured to obtain reliable statistics.

The grain-size distribution of nanograins in IF-steel samples processed by SMAT for 5 min before and after tensile testing at a strain of 0.25 are shown in Fig. S2, which indicates that there is no observable grain growth during the tensile testing.

6. Method to Derive the Mobile Dislocation Density. The mobile dislocation density ρ_m/ρ_{m0} in the current study was measured by repeated stress–relaxation test (2), which exhibits a power variation of dimensionless ρ_m/ρ_{m0} with time (t):

$$\frac{\rho_m}{\rho_{m0}} = \left(\frac{c_r}{t+c_r}\right)^{\beta/(1+\beta)}, \qquad \text{[S1]}$$

where ρ_{m0} is the dislocation density at the start of each transient, c_r is a time constant, and β is a dimensionless immobilization parameter. The derivation of c_r and β is described below.

A single stress–relaxation transient exhibits a logarithmic variation of stress drop with time elapsed. The apparent activation volume V_a can be determined by fitting the logarithmic stress–relaxation curve:

$$\Delta\tau(t) = -\frac{k_B T}{V_a}\ln\left(1+\frac{t}{c_r}\right), \qquad \text{[S2]}$$

where $\Delta\tau(t)$ is the stress drop at time t and k_B is the Boltzmann constant, thus the time constant c_r and apparent activation volume V_a are obtained.

The applied shear stress during plastic deformation could be decomposed into two components: $\tau = \tau_\mu + \tau^*$, where τ_μ is athermal component whereas τ^* is thermally dependent. For the change of thermal component under relaxation condition,

$$\Delta\tau^* = (1 + K^r/M)\Delta\tau, \qquad \text{[S3]}$$

where K^r can be approximated by the strain hardening rate of monotonic tensile curve, and M is the stiffness of specimen–machine assembly.

When plastic flow is governed by thermally activated dislocation glide, the dislocation velocity v depends on activation energy and temperature, which could be described by an Arrhenius-type function:

$$v = f_0 \exp\left(-\frac{\Delta G(\tau^*)}{k_B T}\right), \qquad \text{[S4]}$$

where f_0 is a preexponential constant, and ΔG is the activation energy required to overcome localized obstacles.

From the Orowan equation, the plastic deformation rate $\dot{\gamma}_p$ can be expressed as $\dot{\gamma}_p = \rho_m v b$, where ρ_m is mobile dislocation density and b is the magnitude of the Burgers vector. The physical activation volume is conventionally defined as

$$V^* = -\frac{d\Delta G(\tau^*)}{d\tau^*}. \quad \textbf{[S5]}$$

In repeated stress–relaxation tests, the variation of mobile dislocation density is negligibly small, as the applied stress jumps occurred in short period of time from the end of relaxation 1 to the onset of relaxation 2. Accordingly, the variation of the plastic strain rate is controlled by dislocation velocity given by Eq. **S4**, and thus V^* could be determined by

$$V^* = k_B T \frac{\ln\left(\dot{\gamma}_2^i / \dot{\gamma}_1^f\right)}{\Delta\tau^*}, \quad \textbf{[S6]}$$

where $\dot{\gamma}_2^i$ and $\dot{\gamma}_1^f$ are the shear strain rates at the onset of relaxation 2 and the end of relaxation 1, respectively.

Therefore, the physical activation volume V^* and the parameter $\Omega(=V_a/V^*)$ can be derived from Eqs. **S2** to **S6**. Additionally, it is usually assumed that the mobile dislocation density ρ_m and dislocation velocity v are related by an empirical power law:

$$\frac{\rho_m}{\rho_{m0}} = \left(\frac{v}{v_0}\right)^{\beta}. \quad \textbf{[S7]}$$

Combining Eqs. **S2** to **S7**, the mobile dislocation density of Eq. **S1** is obtained and the dimensionless immobilization parameter β has a type of

$$\beta = \frac{\Omega}{1 + K^r/M} - 1.$$

Finally, the density of retained mobile dislocation (Re) after relaxation could be obtained as $\frac{\rho_m}{\rho_{m0}}\Big|_{t=180\,s}$.

1. Lu K, Lu J (1999) Surface nanocrystallization (SNC) of metallic materials-presentation of the concept behind a new approach. *J Mater Sci Technol* 15:193–197.

2. Caillard D, Martin JL (2003) *Thermally Activated Mechanisms in Crystal Plasticity* (Pergamon, Amsterdam), pp 15–25.

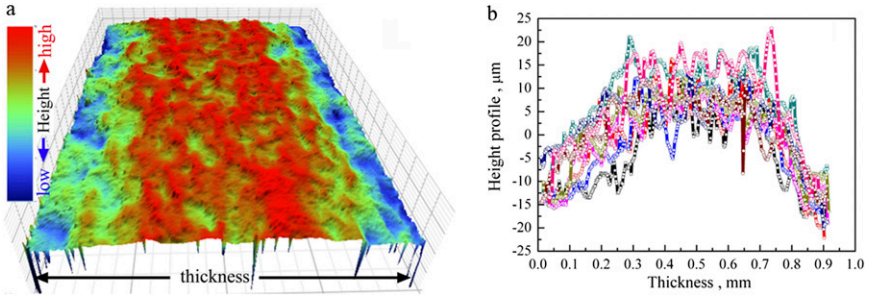

Fig. S1. (*A*) Measured lateral 3D surface topography within the uniform deformation section covering the whole thickness (~0.9 mm) of a GS–CG sample at the tensile strain of 0.25. (*B*) Eight measured height profiles across the lateral surface in *A*, showing evident height differences between the outer layers and inner layer. No height difference exists in the inner layer except for the surface roughness.

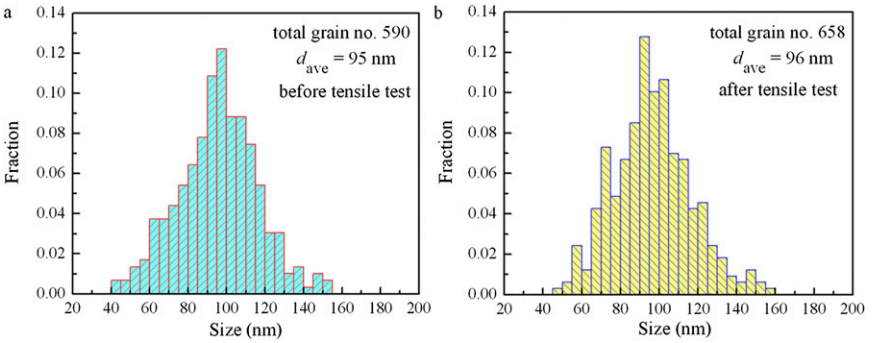

Fig. S2. Statistical distribution of grain sizes at the depth of ~5 μm from the treated surface in IF-steel sample processed by SMAT for 5 min (*A*) before tensile testing and (*B*) after tensile testing at the strain of 0.25.